

2D Materials



PAPER

Narrow plasmon resonances enabled by quasi-freestanding bilayer epitaxial graphene

RECEIVED
19 October 2016

REVISED
11 January 2017

ACCEPTED FOR PUBLICATION
26 January 2017

PUBLISHED
17 February 2017

Kevin M Daniels¹, M Mehdi Jadidi², Andrei B Sushkov³, Anindya Nath⁴, Anthony K Boyd¹, Karthik Sridhara⁵, H Dennis Drew³, Thomas E Murphy², Rachael L Myers-Ward¹ and D Kurt Gaskill¹

¹ US Naval Research Laboratory, Washington, DC 20375, United States of America

² Institute for Research in Electronics & Applied Physics, University of Maryland, College Park, MD 20742, United States of America

³ Center for Nanophysics and Advanced Materials, University of Maryland, College Park, MD 20742, United States of America

⁴ George Mason University, 4400 University Dr, Fairfax, VA 22030, United States of America

⁵ Department of Materials Science and Engineering, Texas A&M University, College Station, TX 77842, United States of America

E-mail: kevin.daniels.ctr@nrl.navy.mil and kurt.gaskill@nrl.navy.mil

Keywords: graphene, terahertz, intercalation, metamaterial, plasmon

Supplementary material for this article is available [online](#)

Abstract

Exploiting the underdeveloped terahertz range ($\sim 10^{12}$ – 10^{13} Hz) of the electromagnetic spectrum could advance many scientific fields (e.g. medical imaging for the identification of tumors and other biological tissues, non-destructive evaluation of hidden objects or ultra-broadband communication). Despite the benefits of operating in this regime, generation, detection and manipulation have proven difficult, as few materials have functional interactions with THz radiation. In contrast, graphene supports resonances in the THz regime through structural confinement of surface plasmons, which can lead to enhanced absorption. In prior work, the achievable plasmon resonances in such structures have been limited by multiple electron scattering mechanisms (i.e. large carrier scattering rates) which greatly broaden the resonance (> 100 cm^{-1} ; 3 THz). We report the narrowest room temperature Drude response to-date, 30 cm^{-1} (0.87 THz), obtained using quasi-free standing bilayer epitaxial graphene (QFS BLG) synthesized on (000 1)6H–SiC. This narrow response is due to a 4-fold increase in carrier mobility and improved thickness and electronic uniformity of QFS BLG. Moreover, QFS BLG samples patterned into microribbons targeting 1.8–5.7 THz plasmon resonances also exhibit low scattering rates (37 – 53 cm^{-1}). Due to the improved THz properties of QFS BLG, the effects of e-beam processing on carrier scattering rates was determined and we found that fabrication conditions can be tuned to minimize the impact on optoelectronic properties. In addition, electrostatic gating of patterned QFS BLG shows narrow band THz amplitude modulation. Taken together, these properties of QFS BLG should facilitate future development of THz optoelectronic devices for monochromatic applications.

Abbreviations

EG	Epitaxial graphene
ML	Monolayer
QFS BLG	Quasi freestanding bilayer epitaxial graphene
XPS	X-ray photoelectron spectroscopy
SEM	Scanning electron microscopy
FTIR	Fourier transform infrared
slm	Standard liters per minute
CNP	Charge neutrality point

Graphene surface plasmons are tightly localized electrons oscillating in a collective motion when excited by an incident electromagnetic wave. Micron-scale graphene structures confine these oscillations,

producing plasmon resonances in the terahertz range and the resonance frequency is tuned electrostatically via an applied gate voltage [1]. In graphene, although the linear dispersion results in a frequency invariant interband absorption of 2.3% in the visible range, radiation in the THz regime is dominated by intraband conductivity which, when coupled to surface plasmons, increases absorption [2]. This latter quality makes graphene attractive for numerous optoelectronic applications in the under-developed THz regime [2–5], including detectors [4, 6–8], emitters [9], modulators [2, 10], antennas [3], switches [5], filters [11] and mixers [12] for communications [13], medical [14, 15], astronomical [16] and security applications [3].

Epitaxial graphene (EG), formed by the sublimation of Si from 4H- or 6H–SiC, is attractive for THz

optoelectronics. Its single crystal nature implies electronically uniform material over large areas [17] an essential requirement for realistic THz devices having $\sim\text{mm}^2$ active areas [18]. In addition, EG THz detectors using dissimilar metal contacts to exploit the hot-electron photothermoelectric effect show encouraging room temperature responsivity with sub-100 ps response times that outperform conventional bolometers operating at low temperatures [4, 19]. Although plasmon resonances can be used to increase detector responsivity, prior studies of terahertz graphene resonances have been hindered by weak absorption, $<10\%$, and large scattering rate, $\gamma > 100\text{ cm}^{-1}$ with $\gamma = 1/2\pi c\tau$, where c is the speed of light and τ is the electronic momentum relaxation time [1, 20–22]. In general, the low Q of EG resonators can be attributed to two obstacles: (1) non-uniformity in thickness due to varying growth rate of EG on the steps and terraces of SiC and (2) charge carrier scattering and resulting low carrier mobility, $\sim 1000\text{ cm}^2\text{ V}^{-1}\text{ s}^{-1}$, caused by the $(6\sqrt{3} \times 6\sqrt{3})\text{ R}30^\circ$ reconstructed carbon layer formed between the Si-terminated (0001) SiC and EG (hereafter the $6\sqrt{3}$ buffer layer) [23, 24]. To help bring graphene THz optoelectronics to fruition, it is necessary to overcome the above obstacles as well as to increase absorption and decrease scattering rate; this requires graphene with high sheet carrier density and high carrier mobility that is homogeneous over $\sim\text{mm}^2$ areas.

The $6\sqrt{3}$ buffer layer forms during the sublimation of Si from (0001) SiC at temperatures above $\sim 1400^\circ\text{C}$ [23]. Furthermore, Si dangling bonds at the interface between the SiC and the buffer layer induce a negative sheet charge density, $n_s \sim 10^{13}\text{ cm}^{-2}$, to the graphene layer [23, 25, 26]. In addition, this buffer layer and proximity to the SiC gives rise to phonon scattering, lowering the mobility with a temperature dependence characteristic of SiC phonons [27–29]. Carrier mobility also depends on n_s where increasing sheet carrier concentration results in a lower mobility [30]. Thus, this $6\sqrt{3}$ buffer layer is a negative interaction for THz plasmonic resonances utilizing EG, resulting in a broadening of the plasmon resonance.

When EG is H-intercalated at $\sim 1000^\circ\text{C}$, hydrogen atoms move between the buffer layer and the (0001) surface passivating the Si dangling bonds and severing the covalent bonds between Si and the C in the buffer layer such that the remaining Si bonds are then bound to hydrogen. The $6\sqrt{3}$ buffer layer is thus promoted to a new layer of EG which is Bernal stacked with respect to the top EG layer and concurrently lifts the graphene layers a small additional distance from the SiC substrate [31] and this combination is QFS BLG. First principle calculations show that the intercalated interface no longer induces charge density to the graphene [32], and instead, the polarization field from the hexagonal substrate induces a p-type charge density of 10^{13} cm^{-2} [33]. The model by Ostler *et al* indicates that H-intercalation only affects the (0001) terraces since the $(1\ 1\ \bar{2}\ 0)$ steps

do not have the $6\sqrt{3}$ buffer layer [23, 29, 34]. Due to the higher growth rate of graphene on the $(1\ 1\ \bar{2}\ 0)$ steps than the (0001) terraces, H-intercalation should result in improved thickness uniformity and reduce carrier scattering from the steps [35, 36]. More importantly, the mobility of quasi-free standing graphene is higher and has a weak temperature dependence, indicating a reduction in phonon-carrier scattering [29]. Thus, QFS BLG should possess traits desirable to advance THz optoelectronics.

We investigated whether improved thickness uniformity can be obtained from H-intercalation. A nominally ‘monolayer’ EG sample was synthesized on SiC, and then, after characterization, H-intercalated (see methods). Figure 1(a) shows the Raman 2D peak full width at half maximum (FWHM) maps of monolayer EG (top) and QFS BLG (bottom). The FWHM of the 2D peak, shown for example in figure 1(b) for typical terraces of monolayer EG and QFS BLG, was used to determine the number of graphene layers, where Bernal stacked 1, 2, and 3 ML corresponds to $\sim 30\text{ cm}^{-1}$, $\sim 55\text{ cm}^{-1}$, and $\sim 75\text{ cm}^{-1}$, respectively [37]; we note little contribution at $\sim 1350\text{ cm}^{-1}$ indicating minimal defects in the films. Statistical analysis of the monolayer EG Raman 2D FWHM map shows 52% 1 ML on the terraces and 41% 2 ML and 7% 3 ML on the steps; this implies the sample had an average thickness of about 1.5 ML, close to the calculated thickness from XPS measurements (1.3 ML) [38]. After H-intercalation, the 2ML and 3ML regions on the $(1\ 1\ \bar{2}\ 0)$ steps remain unchanged, consistent with previous work showing the lack of buffer layer on $(1\ 1\ \bar{2}\ 0)$ SiC [34, 37]. In contrast, EG on (0001) SiC terraces becomes bilayer graphene, demonstrating the promotion of the $6\sqrt{3}$ buffer layer to an additional graphene layer. Analysis of the Raman map reveals that 96% of the sample is bilayer graphene and 4%, found on the steps, is trilayer [31]. Figure 1(c) presents XPS data showing the decoupled nature of QFS BLG from the substrate and XPS calculated thickness is consistent with the bilayer composition [50]. Thus, thickness uniformity has dramatically improved after intercalation, as predicted by the Ostler model. Figure 1(d) illustrates this change in layer thickness with intercalation. The highly uniform bilayer EG on the (0001) terraces is confirmed by SEM, example image in figure 2; the blue, pink, and purple colors correspond to 1, 2, and 3 ML, with noted areal percentages. The discrepancy in areal percentages is due to the higher resolution of SEM ($\sim 50\text{ nm}$) compared to Raman spectroscopy ($\sim 0.6\ \mu\text{m}$) and thus is more sensitive to the presence of small 1 ML areas.

To demonstrate electrical uniformity Hall measurements were performed on different QFS BLG sample sizes: 8 mm, $12\ \mu\text{m}$ (3 devices) and $8\ \mu\text{m}$ (3 devices) squares. The results, summarized in table S1, show little variability with size scaling. The mobility of the different sizes varies by about 3% from the average and sheet density varies by about 8% from the average; these

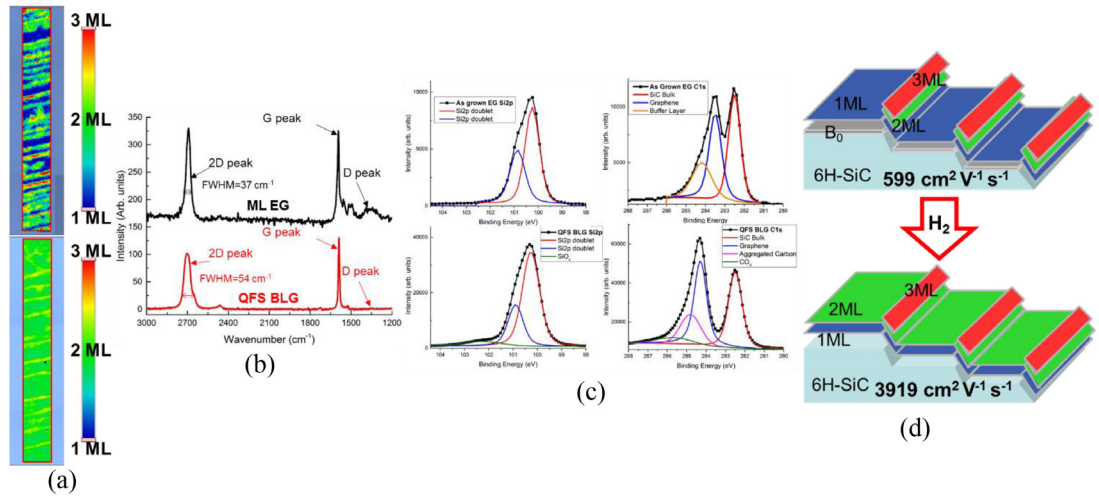


Figure 1. Hydrogen intercalation of EG on SiC (0001): (a) Raman 2D peak full width at half maximum map of EG (top) and QFS BLG (bottom) revealing the promotion of the buffer layer only on the terraces (0001) and not on the steps (11 $\bar{2}$ 0) due to the lack of $6\sqrt{3}$ buffer layer on the steps. (b) Example Raman spectra from the terrace of EG (black) and QFS BLG (red) reveals broadening of the 2D peak of QFS BLG due to the addition of an EG layer upon release of the buffer layer (SiC substrate contributions were subtracted). (c) Si 2p XPS spectra of ML EG (top left) and QFS BLG (bottom left) showing Si 2p doublet of SiC at 100.3 and 100.9 eV. An SiO_x peak is observed in the QFS BLG at 102.3 eV, which may be due to removal and characterization of the sample before intercalation. C 1s XPS spectra of ML EG (top right) shows peaks at 282.5, 283.5 and 284.2 eV correspond to bulk SiC, graphene and buffer layer, respectively. C 1s XPS spectra of QFS BLG (bottom right) shows a prominent component at 284.3 eV for graphene, shifted by 0.8 eV from the graphene peak shown in ML EG, from the change in EG Fermi energy owing to the decoupled nature of QFS BLG from the substrate. A CO_x peak is present at 285.7 eV. While the buffer layer is fully promoted to an EG layer as evident by Raman, the presence of O₂ gives rise to SiO_x which creates excess C from the dissociated SiC as observed by the C 1s peak at 284.8 eV (d) schematic showing (top) the initial layers including buffer layer (B₀), the first graphene layer (G₁), second graphene layer (G₂) and third graphene layer (G₃) and (bottom) the configuration after intercalation where the B₀ becomes G₁ and G₁ becomes G₂. Since there is no $6\sqrt{3}$ buffer layer on the steps, the configuration there does not change after intercalation.

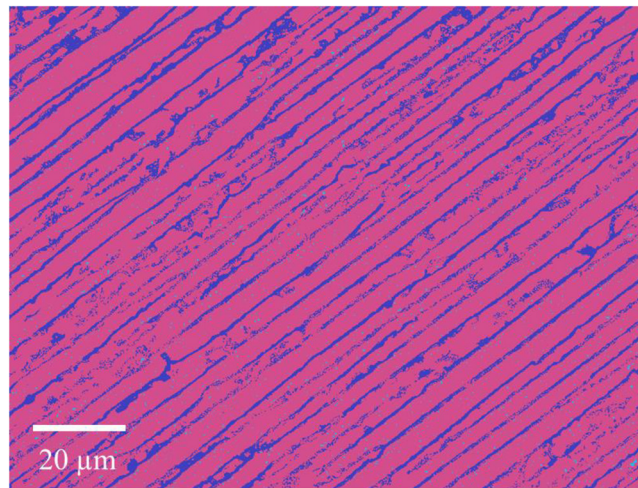


Figure 2. False color SEM of QFS BLG where the blue (2%), pink (90%) and purple (8%), corresponding to 1, 2 and 3 ML, respectively.

values are within experimental error for our set up. We attribute the uniformity of electrical properties of QFS BLG to the improved thickness uniformity.

To probe optical properties, we performed transmission spectroscopy (see Methods) on unpatterned and microribbon grating samples of QFS BLG; see table 1 for sample details. The transmission spectra for unpatterned QFS BLG, Sample A, is shown in figure 3. We analyzed the transmission spectra using the Drude form of the optical conductivity for bilayer graphene, $\sigma_{\text{BLG}}(\omega)$, as shown in equation (1) where E_F is the Fermi

Energy, \hbar is Planck's constant divided by 2π , e is the electronic charge, and γ is related to the relaxation time, τ , and hence carrier mobility, μ , of

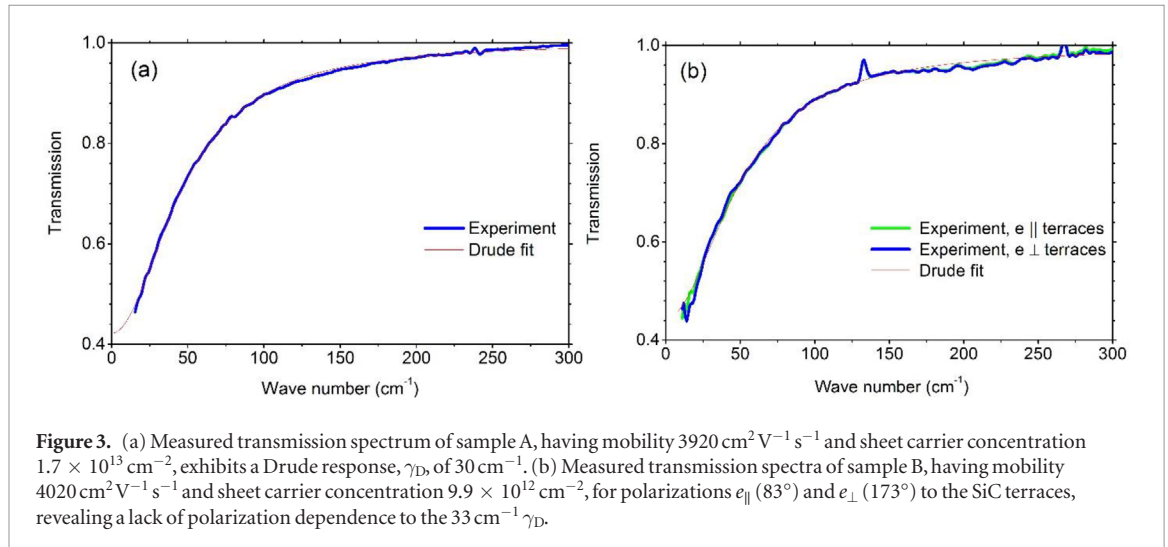
$$\sigma_{\text{BLG}}(\omega) = \sigma_0 \frac{8}{\pi \hbar} \frac{E_F}{1/\tau - i\omega},$$

$$\text{where } \sigma_0 = \frac{e^2}{4\hbar}, \gamma = \frac{1}{2\pi c\tau} \text{ and } \tau = \frac{\mu E_F}{e v_F^2} \quad (1)$$

the sample through the Fermi velocity, v_F [39]. Due to the two graphene layers, $\sigma_{\text{BLG}}(\omega)$ has an additional factor of two compared to that for single layer graphene.

Table 1. Hall mobility, μ , sheet density, n_s , and Drude and plasmon resonance response of unpatterned (UP) and microribbon grating (G) QFS BLG samples.

Sample	μ ($\text{cm}^2 \text{V}^{-1} \text{s}^{-1}$)	n_s (10^{13}cm^{-2})	Grating size (mm^2)	w (μm)	Λ (μm)	γ (UP) (cm^{-2})	γ_D (G) (cm^{-2})	ω_L (G) (cm^{-2})	γ_L (G) (cm^{-2})
A	3920	1.74	—	—	—	30	—	—	—
B	4020	0.989	3×3	7.0	16	33	46	57	46
C	3780	1.06	2×2	1.5	3.0	—	43	129	45
D	3910	0.988	2×2	0.75	1.5	—	63	191	53
E	3850	1.07	1.5×1.5	1.5	3.0	—	—	128	37

**Figure 3.** (a) Measured transmission spectrum of sample A, having mobility $3920 \text{cm}^2 \text{V}^{-1} \text{s}^{-1}$ and sheet carrier concentration $1.7 \times 10^{13} \text{cm}^{-2}$, exhibits a Drude response, γ_D , of 30cm^{-1} . (b) Measured transmission spectra of sample B, having mobility $4020 \text{cm}^2 \text{V}^{-1} \text{s}^{-1}$ and sheet carrier concentration $9.9 \times 10^{12} \text{cm}^{-2}$, for polarizations e_{\parallel} (83°) and e_{\perp} (173°) to the SiC terraces, revealing a lack of polarization dependence to the $33 \text{cm}^{-1} \gamma_D$.

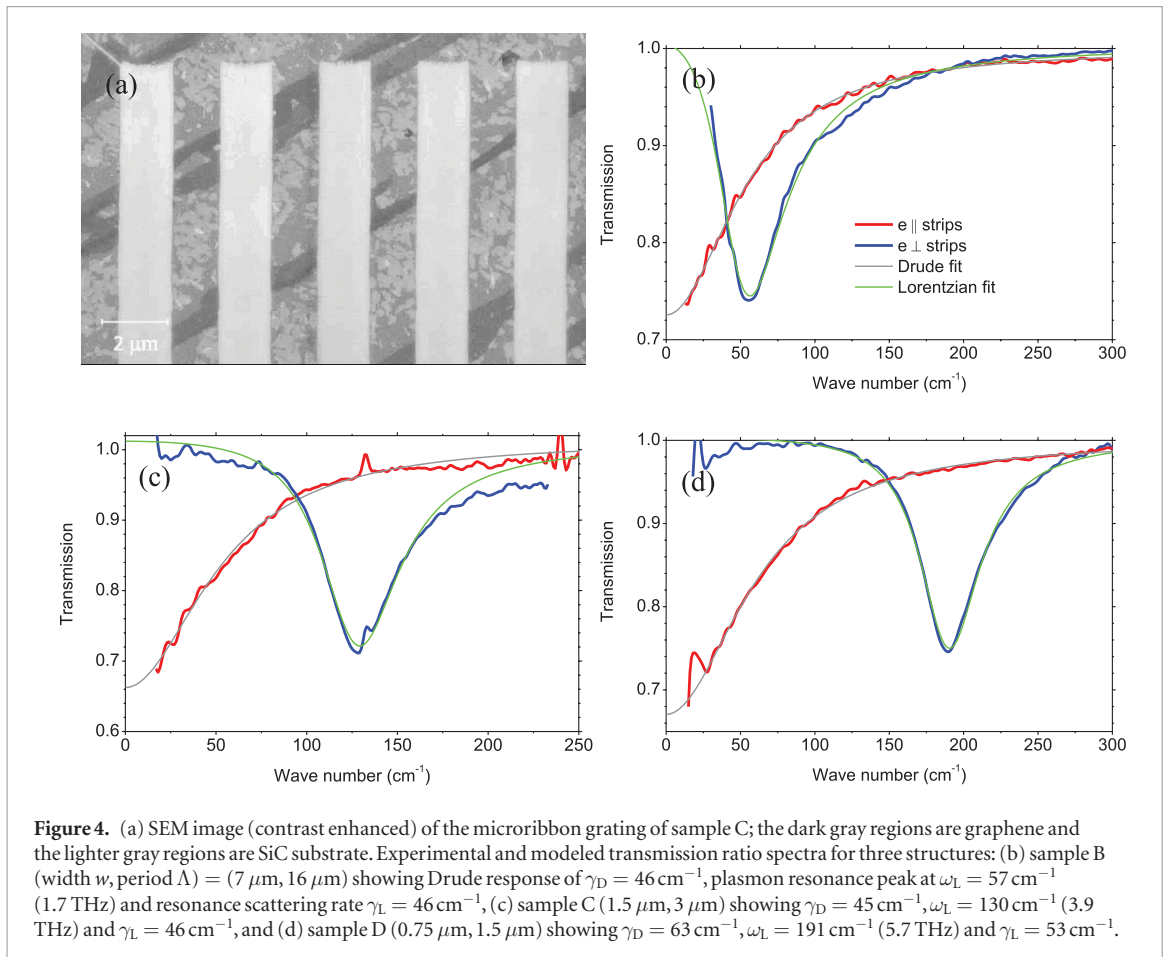
The transmission is well fitted to a single component Drude model, see figure 3(a) (see supplementary information for fitting details). The Drude model fits indicates a γ of 30cm^{-1} , which corresponds to a Drude mobility of $4400 \text{cm}^2 \text{V}^{-1} \text{s}^{-1}$ and is thus consistent with μ of Sample A; this mobility is 4-fold higher than that of EG having similar n_s . Furthermore, the consistency between Drude mobility and μ implies no additional scattering mechanisms are required, i.e. the same physical scattering processes that determine the DC electrical properties fundamentally limit the terahertz optical properties. This is in contrast to previously reported results for chemical vapor deposited graphene on copper, subsequently transferred to SiO_2/Si , where the Drude γ ($\sim 100 \text{cm}^{-1}$) was too large to be due solely to charge-impurity scattering [40]. The consistency between Drude and Hall mobility is further confirmation of the uniformity of electrical properties since the transmission measurement uses a spot size of $\sim 1 \text{mm}^2$. The absorption of QFS BLG, proportional to the real part of the optical conductivity, is about 8-fold higher than that of EG, and a factor of two higher than prior reports for bilayer graphene [41]. This can be understood by considering equation (1); the bilayer composition results in a factor of 2 increase in absorption and since γ is inversely proportional to μ , the optical conductivity for bilayer graphene is further increased about 4-fold.

We also obtained transmission spectra for Sample B, figure 3(b) using an unpatterned area on the sample. Once again, Drude model fits to the transmission spectra

are consistent with the sheet density and mobility of the sample; in this case, γ is 33cm^{-1} . In addition, we acquired transmission spectra at two different polarizations, parallel and perpendicular with respect to the direction of the steps, also shown in figure 3(b), and the data sets nearly overlap each other. Other polarization directions were measured (45° , 135° , and 315° ; not shown) with similar results. This demonstrates that there is no preferential direction to the Drude absorption, consistent with the thickness uniformity established earlier and is in contrast to early reports for quasi-free standing graphene [21]; the difference is most likely due to our careful optimization of the H-intercalation process. In addition, this implies that the presence of steps has minimal impact on the Drude absorption.

We patterned samples B–D into microribbon gratings to confine surface plasmons calculated to have resonances at 60 (1.8), 130 (3.9) and 190 (5.7) cm^{-1} (THz), respectively. Table 1 summarizes sample details and grating dimensions along with the scattering rate from Drude fits, γ_D , and for the resonances, the scattering rate from Lorentzian fits, γ_L . See supplementary information for specifics on the frequency domain finite element method we used to calculate the resonances.

The measured resonant frequency is in remarkable agreement with the calculated frequency for the samples as shown in figure 4, table 1, and in figure S1 (stacks.iop.org/TDM/4/025034/mmedia). In addition, the calculated transmission extinction agrees with measured extinction (compare figure 4 with figure S1). Figure 4(a)



shows an SEM of the microribbon grating for Sample B. The Drude response and resonant plasmon frequency of the graphene gratings are shown in figures 4(b)–(d). The resonances show γ_L (46, 45 and 53 cm^{-1}) similar to the γ_D contributions measured on the same sample yet slightly larger than γ of unpatterned QFS BLG (30–33 cm^{-1}). Dimensional variations could not account for the increased γ_L . (see supplemental information table S2). These results suggest lithographic processing caused the increase in γ_L .

To understand the source of the additional broadening, we fabricated Sample E repeating the dimensions of the microribbon grating of Sample C but using different RIE conditions. Sample E was subjected to O_2 plasma etching with higher power but shorter duration, 100 W at 12 s, compared to 30 W at two 120 s intervals used in the fabrication of the gratings in Samples B through E. The transmission spectra of the Sample E grating, shown in figure 5, had smaller γ_L than the similar grating on Sample C; 37 cm^{-1} versus 46 cm^{-1} . Since γ_L is related to the mobility, it is apparent that the higher total energy dose in etching impacts the electronic properties of the graphene (note that all samples had the same photoresist thickness). Detecting this sensitivity to processing would not have been apparent without the fidelity afforded by the narrow plasmon resonance of QFS BLG.

To confirm our hypothesis that total plasma energy dose has a negative impact on graphene electronic properties, Samples F and G, with similar carrier mobilities

and sheet carrier concentration, were subjected to the O_2 plasma etching conditions of Samples C and E, as detailed in table S3. Sample F, with the highest total energy dose, suffered a 76% drop in mobility compared Sample G, which had only a 47% drop. This implies that fabrication conditions can be optimized to minimize the impact on graphene electronic and THz optoelectronic properties.

Electrostatic gating using an ionic gate on the microribbon grating of Sample D (see methods), as shown in figure 6, showed that the THz resonance frequency can be changed. Gate biases of -2 , -0.5 and 0.25 V were applied to the microribbon grating and the resulting plasmon resonance frequencies were 5.4, 4.9 and 4.5 THz, respectively [1, 42] where the direction of the shift is in accord with the (expected) positive sheet density and the sign of the bias. Due to the demonstrated agreement between theory and experiment presented above, we use the resonance frequencies to calculate the sheet densities for the same bias conditions and find 1.1×10^{13} , 9.0×10^{12} , and $4.7 \times 10^{12} \text{ cm}^{-2}$, respectively. The nearly 2-fold reduction in the extinction for the 0.25 V bias is expected since the extinction is approximately proportional to the E_F through the DC conductivity and E_F (calculated using the sheet density) is reduced nearly 2-fold [6]. Also expected is the broader resonance at 0.25 V since mobility is not expected to change and yet the scattering rate, γ_L , is proportional to E_F^{-1} . We can use the Drude formalism to model γ_L for

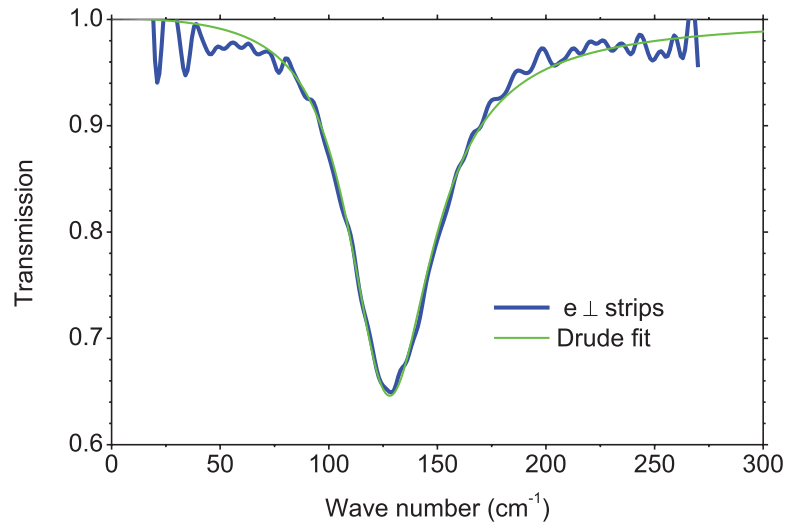


Figure 5. Experimental and modeled transmission ratio spectra for sample E, fabricated with etch parameters of higher power (100 W) but lower duration (12 s). Grating of width (w) = $1.5 \mu\text{m}$, period (Λ) = $3 \mu\text{m}$ showing a plasmon resonance peak at $\omega_L = 128 \text{ cm}^{-1}$ (3.83 THz), and resonance scattering rate $\gamma_L = 37 \text{ cm}^{-1}$. The resonance damping is smaller than sample C ($\gamma_L = 46 \text{ cm}^{-1}$) which has a similar structure but fabricated using higher total energy dose (30 W at 240 s).

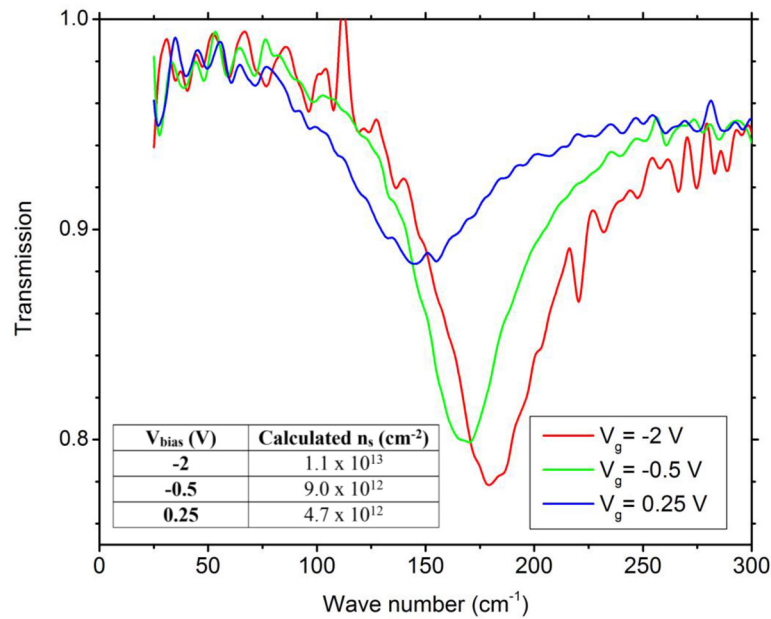


Figure 6. Transmission ratio spectra of sample D using electrolyte gating; the gating voltages and calculated n_s are inset. The plasmon resonance shifted from 190 cm^{-1} to 150 cm^{-1} as the bias was changed from negative to positive, consistent with the reduction in n_s .

a new E_F and find a change of $47\text{--}67 \text{ cm}^{-1}$, consistent with the increase in scattering rate shown in figure 6 [43]. We point out that the low γ_L properties of our non-optimized QFS BLG, and our basic ionic gating approach results imply the potential for relatively narrow transmission amplitude modulation near 200 cm^{-1} (6 THz). Additional improvements in modulation are likely by adjusting the fabrication method to minimize the impact on γ_L and optimizing the gating scheme to achieve larger n_s modulation. More importantly, we believe transmission modulation approaching 100% is realizable by combining QFS BLG with the recently reported metal-contacted plasmon approach [20].

In conclusion, the narrowest terahertz plasmon resonance line width in graphene, 30 cm^{-1} is demonstrated using QFS BLG. This is because hydrogen intercalation results in highly uniform bilayer graphene due to the conversion of the $6\sqrt{3}$ buffer layer to an additional EG layer on the terraces and this buffer layer is absent on the $(1\ 1\ \bar{2}\ 0)$ steps. Hydrogen intercalation also reduces carrier scattering resulting in a 4-fold increase in carrier mobility, with high electrical sample-wide uniformity. Transmission spectra of the unpatterned QFS BLG show no preferential polarization direction further attesting to the thickness and electrical uniformity. Confinement of the surface plasmons through the fabrication

of microribbon gratings show plasmon resonances at frequencies across the THz regime that are in notable agreement with theory. Due to the narrow plasmon resonance observed in our QFS BLG, the effect of processing damage, as a result of the power and duration of the O₂ plasma etch, was determined. The impact of processing can be minimized using, for example, reduced etching power and/or thicker resists. The plasmon resonance is tunable, with the expected bias dependence, and we demonstrate, in principle, narrow band THz amplitude modulation. In general, we find that the properties of QFS BLG meet the requirements for THz optoelectronics and, given the recent advancements in graphene plasmonics, it will enable a wide variety of monochromatic applications such as medical imaging via Terahertz-ray, detection of hazardous gases and explosives or high speed Terabit communications.

Methods

Sample preparation

Nominally monolayer graphene was synthesized from 8 × 8 mm² semi-insulating, (0 0 1)6H-SiC in an Aixtron/Epigress VP508 horizontal hot-wall reactor. The sample is etched in 5 standard liters per minute (SLM) of high purity H₂ (using a laminar flow for this and all of the following) at 200 mbar during a temperature ramp to 1570 °C followed by graphene synthesis in 100 mbar high purity Ar at 1580 °C for 20 min. The reactor is cooled to 950–1150 °C in Ar and H-intercalation of EG is carried out under a flow of 80 slm of H₂ and chamber pressure of 900 mbar for 15–75 min. Optimal temperature and time was determined to be 1050 °C for 60 min using Raman mapping and SEM to confirm material uniformity and Hall measurements for sheet density and carrier mobility [23, 44, 45]. The sample employed for Raman comparison between EG and QFS BLG (figure 2(a)) was first grown without intercalation and removed for characterization, then returned to the reactor, where it is ramped to 1400 °C in Ar in 80 slm of Ar at 200 mbar to desorb any absorbed molecules from exposure to the atmosphere. The sample was then brought to 1050 °C and intercalated with H₂, 80 slm at 900 mbar for 60 min. Reactor temperature calibration using Si melt tests yielded a temperature uniformity of about ±2 K over 100 mm at 1410 °C under a 90 slm H₂ flow.

Sample characterization

A Thermo DXRxi using a 532 nm laser (9.6 mW) with a spot size of ~0.6 μm (100 × objective) was used to acquire 80 μm × 10 μm Raman full width at half maximum maps of the 2D peak at room temperature. SEM was performed using an LEO Supra 55 where differences, in contrast, caused by attenuation of secondary electrons from the substrate by graphene, enables viewing layer number differences [46]. Differences in contrast for the Raman maps and SEM images were statistically analyzed using Image J and

Mathematica to determine areal percentages of mono-, bi-, and trilayer graphene. XPS was performed using a Thermo Scientific K-Alpha XPS with a monochromatic Al-Kα source and spot size of 400 μm area. Four probe, large area (8 × 8 cm²) Hall measurements were executed at room temperature and 2000 G using currents less than 100 μA in a home-built system. AFM measurements used a Bruker Dimension FastScan system.

Structure fabrication

Fabrication began with spin coating two photoresists for deposition of alignment marks. A layer of LOR7B was spun on as LOR is not photosensitive and aids liftoff with minimal residue [47]. Next, a layer of Shipley S1805 was spun on the sample, exposed using a Karl Suss MJB3 mask aligner, and then developed in CD26 developer. After development, a bilayer of Ti(10 nm) and Au(90 nm) was deposited by E-beam evaporation to define metal contacts for gating. The sample was left in PG remover overnight to lift off the excess metal then rinsed with isopropyl alcohol (IPA). A 250 nm layer of ZEP 520 A was spun on, baked, then loaded into a Raith Voyager system where the microribbon grating is defined by E-beam lithography using the fixed beam moving stage (FBMS) setting. After writing the pattern, the sample was developed using ZED N-50 rinsed using IPA and methyl isobutyl ketone. The exposed graphene was etched away using an oxygen plasma in an Oxford Plasmalab reactive ion etcher (RIE) or in a Technics PE II-A Plasma RIE system; conditions were 30 W for two 120 s intervals or 100 W for 12 s. Etching at 100 W for 12 s in the Oxford system was used to test the impact of plasma conditions on graphene electronic properties. The photoresist was removed using PG remover and then rinsed with IPA. Microribbon gratings were isolated using the same procedure. AFM and SEM was used to measure variations in microribbon width. The microribbon was then ionically gated by drop-casting ethylene oxide and lithium perchlorate (LiClO₄) onto the sample and making contact to the aforementioned Ti–Au contact pad; this approach has been successfully used to probe plasmonic resonances in graphene [6]. Electron doping of the graphene, due to the electrolyte, was observed. This is ascribed to Li⁺ adsorption, shifting the charge neutrality point by –2 V [48]. Capacitance of the ionic gate is constant across the sample and thickness invariant, as capacitance is dominated by the monolayer of ions forming the Debye layer [49].

FTIR measurement

Room temperature far infrared measurements used a Bomem DA-8 FTIR spectrometer with a mercury lamp as a source and a 4 K silicon composite bolometer as a detector; the spot size was ~1 mm and is smaller than the microribbon gratings dimension. Sample and reference SiC substrate were glued to identical Cu circular apertures inscribed into square graphene structure. THz beam illuminates the substrate side of

the sample. A rotating polarizer in front of the sample was used for transmission measurements with the electric field of light parallel and perpendicular to graphene strips, which yield the plasmonic and Drude responses. Transmission in figures 3–5 is defined as the raw transmission spectra of the graphene on SiC divided by the raw transmission spectra of bare SiC. The aforementioned transmission ratios were corrected by the transmission ratio of the empty holes.

Acknowledgment

This research was performed while Kevin M Daniels held an NRC Research Associateship award at the US Naval Research Laboratory. This research was performed while A K Boyd held an American Society for Engineering Education postdoctoral fellowship at the US Naval Research Laboratory. Work at the US Naval Research Laboratory was supported by the Office of Naval Research. The authors would like to thank Dmitry Kozak for assisting in the fabrication of the gratings and Virginia Anderson for taking XPS of samples.

Author contributions

K M Daniels, M M Jadidi, A B Sushkov, H D Drew, A K Boyd, T E Murphy, and D K Gaskill conceived the experiment. K M Daniels, A K Boyd, R L Myers-Ward, and D K Gaskill synthesized graphene on SiC. M M Jadidi designed microribbon arrays. K M Daniels took Raman maps and analyzed the data. A K Boyd performed SEM characterization on samples. R L Myers-Ward did XPS and analyzed spectra to determine layer thickness. A B Sushkov and M M Jadidi performed the THz measurement. M M Jadidi performed the gated FTIR measurement. A Nath, A K Boyd and M M Jadidi fabricated the microribbon gratings. K Sridhara created the false color SEM image and used statistical analysis to determine thickness percentages from Raman and SEM. The manuscript was written through contributions of all authors. All authors have given approval to the final version of the manuscript.

Funding sources

The work performed at NRL was supported by the Office of Naval Research. This work was sponsored by the U.S. ONR (N000141310865) and the U.S. NSF (ECCS 1309750).

References

- [1] Ju L *et al* 2011 Graphene plasmonics for tunable terahertz metamaterials *Nat. Nanotechnol.* **6** 630–4
- [2] Sensale-Rodriguez B, Yan R, Kelly M M, Feng T, Tahy K, Hwang W S, Jena D and Xing H G 2012 Broadband graphene terahertz modulators enabled by intraband transitions *Nat. Commun.* **3** 780
- [3] Vicarelli L, Vitiello M S, Coquillat D, Lombardo A, Ferrari A C, Knap W, Polini M, Pellegrini V and Tredicucci A 2012 Graphene field-effect transistors as room-temperature terahertz detectors *Nat. Mater.* **11** 865–71
- [4] Cai X *et al* 2014 Sensitive room temperature terahertz detection via the photothermoelectric effect in graphene *Nat. Nanotechnol.* **9** 814–9
- [5] Lee S H *et al* 2012 Switching terahertz waves with gate-controlled active graphene metamaterials *Nat. Mater.* **11** 936–941
- [6] Cai X, Sushkov A B, Jadid M M, Nyakiti L O, Myers-Ward R L, Gaskil D K, Murphy T E, Fuhrer M S and Drew H D 2015 Plasmon-enhanced terahertz photodetection in graphene *Nano Lett.* **15** 4295–302
- [7] Fatimy A E, Myers-Ward R L, Boyd A K, Daniels K M, Gaskil D K and Barbara P 2016 Epitaxial graphene quantum dots for high-performance terahertz bolometers *Nat. Nanotechnol.* **11** 335–8
- [8] Rogalsky A 2011 Terahertz detectors and focal plane arrays *Opto-Electron. Rev.* **19** 346–404
- [9] Brar V W, Sherrott M C, Jang M S, Kim S, Kim L, Choi M, Sweatlock L A and Atwater H A 2015 Electronic modulation of infrared radiation in graphene plasmonic resonators *Nat. Commun.* **6** 7032
- [10] Yan H, Li X, Chandra B, Tulevski G, Wu Y, Freitag M, Zju W, Avouris P and Xia F 2012 Tunable infrared plasmonic devices using graphene/insulator stacks *Nat. Nanotechnol.* **7** 330–4
- [11] Li J H, Wang L L, Liu J Q, Huang Z R, Sun B and Zhai X 2014 Investigation of the graphene based planar plasmonic filters *J. Appl. Phys.* **103** 211104
- [12] Mizuji E G, Abdolali A, Aghamohamadi F, Danaeifar M, Hashemi S and Tehrani K N 2014 Realization of THz band mixer using graphene *Adv. Electromagn.* **3** 15–9
- [13] Akyildiz I F, Jornet J M and Han C 2014 Terahertz band: next frontier for wireless communications *Phys. Commun.* **12** 16–32
- [14] Wilmink G J and Grundt J E 2011 Current state of research on biological effects of terahertz radiation *J. Infrared Milli Terahz Wave* **32** 1074–122
- [15] Rodrigo D, Limaj O, Janner D, Etezadi D, Abajo F J G, Pruneri V and Altug H 2015 Mid-infrared plasmonic biosensing with graphene *Science* **349** 165–8
- [16] Choudhury B, Sonde A and Jha M R 2016 *Terahertz Antenna Technology for Space Applications* (Berlin: Springer) pp 1–33
- [17] Phaedon A and Dimokratopoulos C 2012 Graphene: synthesis and applications *Mater. Today* **15** 86–97
- [18] Chan W L, Deibel J and Mittleman D M 2007 Imaging with terahertz radiation *Rep. Prog. Phys.* **70** 1325–79
- [19] Tielrooij K J, Massicotte M, Piatkowski L, Woessner A, Ma Q, Jarillo-Herrero P, van Hulst N F and Koppens F H L 2015 Hot-carrier photocurrent effects at graphene-metal interfaces *J. Phys.: Condens. Matter* **27** 164207
- [20] Jadidi M M, Sushkov A B, Myers-Ward R L, Boyd A K, Daniels K M, Gaskil K D, Fuhrer M S, Drew H D and Murphy T E 2015 Tunable terahertz hybrid metal-graphene plasmons *Nano Lett.* **15** 7099–104
- [21] Carassee I, Orlita M, Potemski M, Walter A L, Ostler M, Seyller T, Gaponenko I, Chen J and Kuzmenko A B 2012 Intrinsic terahertz plasmons and magnetoplasmons in large scale monolayer graphene *Nano Lett.* **12** 2470–4
- [22] Nikitin A Y, Guinea F, Garcia-Vidal F J and Martin-Moreno L 2011 Edge and waveguide terahertz surface plasmon modes in graphene microribbons *Phys. Rev. B* **84** 161407
- [23] Riedl C, Coletti C and Starke U 2010 Structural and electronic properties of epitaxial graphene on SiC(0001): a review of growth, characterization, transfer doping and hydrogen intercalation *J. Phys. D: Appl. Phys.* **43** 374009
- [24] Emtsev K V, Speck F, Seyller T and Ley L 2008 Interaction, growth, and ordering of epitaxial graphene on SiC {0001} surfaces: a comparative photoelectron spectroscopy study *Phys. Rev. B* **77** 155303
- [25] Daas B, Omar S U, Shetu S, Daniels K M, Ma S, Sudarshan T S and Chandrashekhara M 2012 Comparison of epitaxial

- graphene growth on polar and nonpolar 6H-SiC faces: on the growth of multilayer films *Cryst. Growth Des.* **12** 3379–87
- [26] Varchon F *et al* 2007 Electronic structure of epitaxial graphene layers on SiC: effect of the substrate *Phys. Rev. Lett.* **99** 126805
- [27] Tanabe S, Sekine Y, Kageshima H, Magase M and Hibino H 2011 Carrier transport mechanism in graphene on SiC (0001) *Phys. Rev. B* **84** 115458
- [28] Hibino H, Tanabe S, Mizuno S and Kageshima H 2012 Growth and electronic transport properties of epitaxial graphene on SiC *J. Phys. D: Appl. Phys.* **45** 154008
- [29] Speck F, Jobst J, Fromm F, Ostler M, Waldmann D, Weber H B and Seyller T 2011 The quasi-free-standing nature of graphene on H-saturated SiC (0001) *Appl. Phys. Lett.* **99** 112106
- [30] Tedesco J L *et al* 2009 Hall effect mobility of epitaxial graphene grown on silicon carbide *Appl. Phys. Lett.* **95** 112102
- [31] Emery J D, Wheeler V D, Johns J E, McBriarty M E, Detlefs B, Hersam M C, Gaskill D K and Bedzyk M J 2014 Structural consequences of hydrogen intercalation of epitaxial graphene on SiC (0001) *Appl. Phys. Lett.* **105** 161602
- [32] Jayasekera T, Xu S, Kim W and Nardelli M B 2011 Electronic properties of the graphene/6H-SiC(000-1) interface: A first-principles study *Phys. Rev. B* **84** 035442
- [33] Ristein J, Mammadov S and Seyller T 2012 Origin of doping in quasi-free-standing graphene on silicon carbide *Phys. Rev. Lett.* **108** 246104
- [34] Ostler M, Deretzis I, Mammadov S, Giannazzo F, Nicoritra G, Spinella C, Seyller T and La Magna A 2013 Direct growth of quasi-free-standing epitaxial graphene on nonpolar SiC surfaces *Phys. Rev. B* **88** 085408
- [35] Yakes M K, Gunlycke D, Tedesco J L, Campbell P M, Myers-Ward R L, Eddy C R, Gaskill D K, Sheehan P E and Laracuente A R 2010 Conductance anisotropy in epitaxial graphene sheets generated by substrate interactions *Nano Lett.* **10** 1559–62
- [36] Ji S, Hannon J B, Tromp R M, Perebeinos V, Tersoff J and Ross F M 2012 Atomic-scale transport in epitaxial graphene *Nat. Mater.* **11** 114–9
- [37] Lee D S, Riedl C, Krauss B, von Klitzing K, Starke U and Smet J H 2008 Raman spectra of epitaxial graphene on SiC and of epitaxial graphene transferred to SiO₂ *Nano Lett.* **8** 4320–5
- [38] Cumpson P J 2000 The thickogram: a method for easy film thickness measurement in XPS *Surf. Interface Anal.* **29** 403–6
- [39] Sorger C, Preu S, Schmidt J, Winnerl S, Bludov Y V, Peres N M R, Vasilevskiy M I and Weber H B 2015 Terahertz response of patterned epitaxial graphene *New J. Phys.* **17** 053045
- [40] Horng J *et al* 2011 Drude conductivity of Dirac fermions in graphene *Phys. Rev. B* **83** 165113
- [41] Suzuki S, Takamura M and Yamamoto H 2016 Transmission, reflection, and absorption spectroscopy of graphene microribbons in the terahertz region *Japan. J. Appl. Phys.* **55** 06GF08
- [42] Kim J, Son H, Cho D J, Geng B, Regan W, Shi S, Kim K, Zettl A, Shen Y R and Wang F 2012 Electrical control of optical plasmon resonance with graphene *Nano Lett.* **12** 5598–602
- [43] Luo X, Qiu T, Lu W and Ni Z 2013 Plasmons in graphene: recent progress and applications *Mater. Sci. Eng. R* **74** 351–76
- [44] Nyakiti L, Wheeler V, Garces N, Myers-Ward R, Eddy C R Jr and Gaskill D K 2012 Enabling graphene-based technologies: toward wafer-scale production of epitaxial graphene *MRS Bull.* **37** 1149–57
- [45] Robinson J A, Hollander M, Cavalero R, Labella M, Trumbull K A and Snyder D W 2011 Epitaxial graphene transistors: enhancing performance via hydrogen intercalation *Nano Lett.* **11** 3875–80
- [46] Kochat V, Pal A N, Sneha E S, Sampathkumar A, Gairola A, Shivashankar S A, Raghavan S and Ghosh A 2011 High contrast imaging and thickness determination of graphene with in-column secondary electron microscopy *J. Appl. Phys.* **110** 014315
- [47] Nath A *et al* 2014 Achieving clean epitaxial graphene surfaces suitable for device applications by improved lithographic process *Appl. Phys. Lett.* **104** 224102
- [48] Pachoud A, Jaiswal M, Ang P K, Loh K P and Ozyilmaz B 2010 Graphene transport at high carrier densities using a polymer electrolyte gate *EPL* **92** 27001
- [49] Badhwar S, Sibik J, Kidambi P R, Beere H E, Zeitler J A, Hofmann S and Ritchie D A 2013 Intrinsic terahertz plasmon signatures in chemical vapour deposited graphene *Appl. Phys. Lett.* **103** 121110
- [50] Oliveria M H Jr, Schumann T, Fromm F, Koch R, Ostler M, Ramsteiner M, Seyller T, Lopes J M J and Riechert H 2013 Formation of high-quality quasi-free-standing bilayer graphene on SiC(0001) by oxygen intercalation upon annealing in air *Carbon* **52** 83–9